Reconstruction of primordial tensor power spectra from *B*-mode polarization of the cosmic microwave background

Takashi Hiramatsu,[1] Eiichiro Komatsu,[2,3] Masashi Hazumi,[3,4,5,6] and Misao Sasaki[7,8]

[1]*Department of Physics, Rikkyo University, Toshima, Tokyo 171-8501, Japan*
[2]*Max-Planck-Institut für Astrophysik, Karl-Schwarzschild Strasse 1, 85748 Garching, Germany*
[3]*Kavli Institute for the Physics and Mathematics of the Universe (Kavli IPMU, WPI), Todai Institutes for Advanced Study, the University of Tokyo, Kashiwa 277-8583, Japan*
[4]*High Energy Accelerator Research Organization (KEK), Tsukuba, Ibaraki 305-0801, Japan*
[5]*SOKENDAI (The Graduate University for Advanced Studies), Hayama, Miura District, Kanagawa 240-0115, Japan*
[6]*Institute of Space and Astronautical Science (ISAS), Japan Aerospace Exploration Agency (JAXA), Sagamihara, Kanagawa 252-0222, Japan*
[7]*Center for Gravitational Physics, Yukawa Institute for Theoretical Physics, Kyoto University, Kyoto 606-8502, Japan*
[8]*International Research Unit of Advanced Future Studies, Kyoto University, Kyoto 606-8502, Japan*

(Received 14 March 2018; published 11 June 2018)

Given observations of the *B*-mode polarization power spectrum of the cosmic microwave background (CMB), we can reconstruct power spectra of primordial tensor modes from the early Universe without assuming their functional form such as a power-law spectrum. The shape of the reconstructed spectra can then be used to probe the origin of tensor modes in a model-independent manner. We use the Fisher matrix to calculate the covariance matrix of tensor power spectra reconstructed in bins. We find that the power spectra are best reconstructed at wave numbers in the vicinity of $k \approx 6 \times 10^{-4}$ and 5×10^{-3} Mpc^{-1}, which correspond to the "reionization bump" at $\ell \lesssim 6$ and "recombination bump" at $\ell \approx 80$ of the CMB *B*-mode power spectrum, respectively. The error bar between these two wave numbers is larger because of the lack of the signal between the reionization and recombination bumps. The error bars increase sharply toward smaller (larger) wave numbers because of the cosmic variance (CMB lensing and instrumental noise). To demonstrate the utility of the reconstructed power spectra, we investigate whether we can distinguish between various sources of tensor modes including those from the vacuum metric fluctuation and SU(2) gauge fields during single-field slow-roll inflation, open inflation, and massive gravity inflation. The results depend on the model parameters, but we find that future CMB experiments are sensitive to differences in these models. We make our calculation tool available online.

DOI: 10.1103/PhysRevD.97.123511

I. INTRODUCTION

Primordial gravitational waves from the very early Universe generate *B*-mode polarization in the cosmic microwave background (CMB) [1,2]. Usually, we calculate the angular power spectrum of *B*-mode polarization by assuming a specific form (e.g., a power law) of the power spectrum of gravitational waves (tensor perturbations) in the early Universe and numerically evolving tensor perturbations forward with a linear Boltzmann code such as CMBFAST[1] [3], CAMB[2] [4], and CLASS[3] [5].

It is also possible to reconstruct initial tensor power spectra in bins of wave numbers from an observed CMB *B*-mode power spectrum. This is possible when the transfer function that relates the initial (primordial) tensor power to that at late times depends only on the standard cosmological parameters and not on the nature of initial tensor perturbations. In this paper, we use inflation [6–11] as an example.

Inflation can produce primordial tensor perturbations from either the vacuum fluctuation in the metric [12] or matter fields (see, e.g., Ref. [13] and references therein). The vacuum metric fluctuation in single-field slow-roll inflation models typically yields a nearly scale-invariant tensor power spectrum [14], whereas the sourced tensor modes can be strongly scale dependent [13]. In addition, tensor perturbations from open inflation [15] and massive gravity inflation (see, e.g., Ref. [16] and references therein and also see Appendix A) can produce scale-dependent tensor perturbations. It is always possible to test these

[1]https://lambda.gsfc.nasa.gov/toolbox/tb_cmbfast_ov.cfm.
[2]https://camb.info/.
[3]http://class-code.net/.

models individually by assuming a functional form of the initial tensor power spectrum, evolving it forward, and comparing to the observed B-mode power spectrum; however, reconstructing the tensor power spectrum from the observed B-mode power spectrum allows us to directly test various sources of the tensor perturbation. In addition, as the reconstruction does not depend on the nature of initial tensor perturbations, it may reveal unexpected features in the initial tensor power spectrum in a model-independent manner. In this paper, we demonstrate this point using the Fisher matrix formalism.

The rest of the paper is organized as follows. In Sec. II, we describe our methodology. In Sec. III, we obtain the covariance matrix of the reconstructed tensor power spectrum and show how to distinguish between various models. We conclude in Sec. IV.

II. METHODOLOGY

We parametrize the primordial tensor power spectrum by N bins in logarithmic intervals,

$$\mathcal{P}_h(k) = \begin{cases} \mathcal{P}_h^{\rm fid}(k) + \delta\mathcal{P}_i & \text{for } k_{i-1} \le k < k_i \text{ with } 1 \le i \le N, \\ \mathcal{P}_h^{\rm fid}(k) & \text{for } k < k_0 \text{ and } k_N \le k, \end{cases} \tag{1}$$

where $\mathcal{P}_h(k) = (k^3/2\pi^2)P_h(k)$ is the dimensionless amplitude of the tensor power spectrum, $\delta\mathcal{P}_i$'s are constants, and $k_n = \alpha^n k_0$ with a constant α controlling the logarithmic interval. In this paper, we shall take a power-law spectrum as the fiducial power spectrum $\mathcal{P}_h^{\rm fid}(k)$,

$$\mathcal{P}_h^{\rm fid}(k) = r\mathcal{P}_{\mathcal{R}0}\left(\frac{k}{k_{\rm pivot}}\right)^{n_T}, \tag{2}$$

where r is the tensor-to-scalar ratio and $\mathcal{P}_{\mathcal{R}0}$ is the amplitude of curvature perturbations at the pivot scale, $k = k_{\rm pivot} = 0.002\ {\rm Mpc}^{-1}$.

We use the Fisher matrix to compute the covariance matrix of $\delta\mathcal{P}_i$ given measurement uncertainties in the B-mode observations. The Fisher matrix is given by

$$F_{ij} = f_{\rm sky}\sum_{\ell=2}^{\ell_{\rm max}} \frac{2\ell+1}{2}\frac{1}{\mathcal{N}_\ell^2}\left(\frac{\partial C_\ell^{\rm BB}}{\partial\delta\mathcal{P}_i}\right)\left(\frac{\partial C_\ell^{\rm BB}}{\partial\delta\mathcal{P}_j}\right), \tag{3}$$

where $f_{\rm sky}$ is a fraction of the sky observed, and

$$\frac{\partial C_\ell^{\rm BB}}{\partial\delta\mathcal{P}_i} = 4\pi\int_{k_{i-1}}^{k_i} T_{B\ell}^{(T)2}(k)\frac{dk}{k}, \tag{4}$$

with the tensor B-mode transfer function $T_{B\ell}^{(T)}$.

TABLE I. Fiducial cosmological parameters provided by Planck 2015 results (TT, TE, EE + lowP + lensing + ext in Ref. [17]).

Amplitude of curvature perturbation	$\mathcal{P}_{\mathcal{R}0}$	2.441×10^{-9}
Pivot scale	$k_{\rm pivot}$	$0.002\ {\rm Mpc}^{-1}$
Spectral index	n_s	0.9667
Reduced Hubble parameter	h	0.6774
Dark matter fraction	$h^2\Omega_{\rm CDM}$	0.1188
Baryon fraction	$h^2\Omega_{\rm b}$	0.02230
Effective number of neutrinos	$N_{\rm eff}$	3.046
Photon's temperature	$T_{\gamma,0}$	2.7255 K
Optical depth	τ	0.066
Helium abundance	Y_p	0.24667

As for the noise contributions, we use

$$\mathcal{N}_\ell = C_\ell^{\rm BB,fid} + \lambda C_\ell^{\rm BB,lens} + N_\ell \exp(\ell^2\sigma_b^2). \tag{5}$$

Here, $C_\ell^{\rm BB,fid}$ is the angular power spectrum of B-mode polarization from the fiducial tensor power spectrum:

$$C_\ell^{\rm BB,fid} = 4\pi\int T_{B\ell}^{(T)2}(k)\mathcal{P}_h^{\rm fid}(k)\frac{dk}{k}. \tag{6}$$

We use CMB2ND to compute the transfer function with the cosmological parameters from the Planck 2015 results (TT, TE, EE + lowP + lensing + ext in Ref. [17]), which are tabulated in Table I. We have checked that the results of CMB2ND and CAMB agree precisely.

The second term in Eq. (5), $C_\ell^{\rm BB,lens}$, is the contribution from CMB lensing [18]. The parameter λ is a "delensing factor," being 0 if the lensing effect is completely removed. The lensing B mode induced by the scalar perturbations is given by (e.g., see Ref. [19] and references therein)

$$C_\ell^{\rm BB,lens} = \frac{1}{2\ell+1}\sum_{\ell' L}^{\ell'_{\rm max}} (\mathcal{S}_{\ell\ell' L}^{(-)})^2 C_{\ell'}^{\rm EE} C_L^{\phi\phi}, \tag{7}$$

where $C_\ell^{\rm EE}$ is the angular power spectrum of the E mode induced by scalar perturbations and $C_\ell^{\phi\phi}$ is that of the lensing potential [20]. To obtain $C_\ell^{\rm BB,lens}$ for $\ell \le 500$ with sufficient accuracy, we sum the right-hand side up to $\ell'_{\rm max} = 2000$. We find that our $C_\ell^{\rm BB,lens}$ agrees with that of CAMB to within 0.2% accuracy at $\ell = 120$, and the error exceeds 1% for $\ell \ge 1208$. The factor $\mathcal{S}_{\ell\ell' L}^{(-)}$ is defined as

$$\mathcal{S}_{\ell\ell' L}^{(-)} \equiv \sqrt{\frac{(2\ell+1)(2\ell'+1)(2L+1)}{16\pi}} \times [-\ell(\ell+1) + \ell'(\ell'+1) + L(L+1)] \times \begin{pmatrix} \ell & \ell' & L \\ 2 & -2 & 0 \end{pmatrix}. \tag{8}$$

Note that $\mathcal{S}^{(-)}_{\ell\ell' L}$ is zero unless $\ell + \ell' + L$ is odd. Finally, the third term in Eq. (5), N_ℓ, is the instrumental noise multiplied by the effect of beam smearing with a width of σ_b. Here, we assume that N_ℓ is white noise given by [21]

$$N_\ell = \left(\frac{\pi}{10800}\frac{w_p^{-1/2}}{\mu\mathrm{K\,arc\ min}}\right)^2 \mu\mathrm{K}^2\ \mathrm{str}. \tag{9}$$

In the actual observations, N_ℓ depends on ℓ because of, e.g., $1/f$ noise and residual foreground emission. The foreground contribution can be included partially by increasing N_ℓ from the instrumental noise level. The ℓ-dependent foreground residual can be incorporated by following, e.g., Appendix C of Ref. [22]; however, we shall ignore the ℓ-dependent noise in this paper.

We truncate the summation at $\ell_{\rm max} = 500$. We have confirmed that the main results are not sensitive to the exact choice of $\ell_{\rm max}$ as long as we have $\ell_{\rm max} > 100$. This is because the primordial B mode decays at $\ell \gtrsim 80$, whereas the noise and lensing B mode dominate at large ℓ.

In this paper, we assume a 0.5 degree full width at half maximum (FWHM) beam (e.g., LiteBIRD [23]), $\sigma_b = 0.5\pi/180\sqrt{8\ \ln 2} = 3.7 \times 10^{-3}$. We define three noise models: (a) a low-noise model with $(w_p^{-1/2}, \lambda) = (1\ \mu\mathrm{K}\cdot\mathrm{arc\ min}, 1)$; (b) a high-noise model with $(w_p^{-1/2}, \lambda) = (10\ \mu\mathrm{K}\cdot\mathrm{arc\ min}, 1)$; and (c) a delensed model with $(w_p^{-1/2}, \lambda) = (1\ \mu\mathrm{K}\cdot\mathrm{arc\ min}, 0)$. As the lensed B-mode power spectrum at $\ell \ll 10^3$ is approximately the same as that of white noise with 5 $\mu\mathrm{K}\cdot\mathrm{arc\ min}$ [20], the variance at high multipoles for case (a) is dominated by lensing, whereas that for case (b) is dominated by noise. Case (c) is nearly an ideal case with complete delensing,

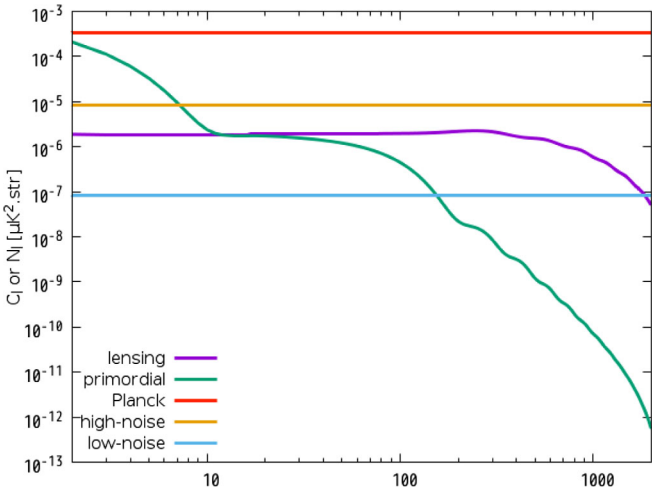

FIG. 1. Noise sources assumed in Eq. (5) for which we consider the cosmic variance (green), lensing effect of scalar perturbations (purple), and the white noise with $w_p^{-1/2} = 1$ (cyan), 10 (orange), and 63.1 $\mu\mathrm{K}\cdot\mathrm{arc\ min}$ (red), dubbed as "low-noise," "high-noise," and "Planck noise" models, respectively.

which would be unrealistic but should serve as a useful reference. The amplitudes of each noise source in Eq. (5) are shown in Fig. 1.

The inverse of the Fisher matrix gives a covariance matrix of the reconstructed tensor power spectra. The diagonal elements give 1σ uncertainties of $\delta\mathcal{P}_i$ at each bin,

$$\sigma^2_{\delta\mathcal{P}_i} = (F^{-1})_{ii},. \tag{10}$$

III. RESULTS

Throughout this paper, we set $f_{\rm sky} = 1$. In Fig. 2, we show $\sigma_{\delta\mathcal{P}_i}$ [Eq. (10)] for $(r, n_T, k_0, k_N, N, \alpha) = (0.01, 0, 10^{-4}\ \mathrm{Mpc}^{-1}, 3\times10^{-2}\ \mathrm{Mpc}^{-1}, 8, 2.04)$. The solid line shows the fiducial spectrum $\mathcal{P}_h^{\rm fid}$. Each box shows the 1σ region around the fiducial spectrum. On large scales, the uncertainty is mainly due to the cosmic variance. On small scales, the contributions from noise and lensing dominate. The covariance matrix including off-diagonal terms is given in Table II.

We find that the tensor power spectra are best reconstructed at two wave number bins around $k \approx 6\times10^{-4}$ and $5\times10^{-3}\ \mathrm{Mpc}^{-1}$. While the precise wave numbers at which the spectra are best constrained depend on the choice of bin sizes, we can understand these values analytically. The B-mode power spectrum of CMB polarization has two characteristic scales: the so-called reionization bump at $\ell \lesssim 6$ and the recombinatiom bump at $\ell \approx 80$. The wave number that gives the former is $k_{\rm reion} \approx 3/[r_L - r(z_{\rm reion})]$ [24], where $r_L = 14$ Gpc and $r(z_{\rm reion}) \approx 9$ Gpc are the comoving distances to the surface of last scatter and the epoch of reionization, e.g., $z_{\rm reion} \approx 8$. We thus obtain $k_{\rm reion} \approx 6\times10^{-4}\ \mathrm{Mpc}^{-1}$. The wave number that gives the latter is $k_{\rm recomb} \approx 80/r_L \approx 6\times10^{-3}\ \mathrm{Mpc}^{-1}$.

Usually, the 1σ regions shrink as we go to higher wave numbers at which the number of modes is greater; however, we find in Fig. 2 an unusual feature that the 1σ regions shrink first, increase at $k \approx 10^{-3}\ \mathrm{Mpc}^{-1}$, and shrink again at $k \gtrsim 2\times10^{-3}\ \mathrm{Mpc}^{-1}$. This is due to a gap (i.e., lack of the signal) between the reionization and recombination bumps. The transfer function leaves only a small B-mode signal here, making reconstruction of the initial tensor power spectrum noisy. With these, we understand all the features in Fig. 2.

Can we distinguish between various models of the source of tensor modes from inflation? In Fig. 2, we show some theoretical predictions of the tensor power spectrum from an SU(2)-axion model with $(r_*, k_p, \sigma) = (0.05, 2.0\times10^{-3}\ \mathrm{Mpc}^{-1}, 0.4)$, from a massive gravity inflation model with $(\alpha, \beta, T_R, g_{*S}, N_*, n_{T*}) = (0.7, 1.0, 10^{10}\ \mathrm{GeV}, 100, 47, 0)$ (see Appendix A), and from a red-tilted spectrum on large scales with $\mathcal{P}(k) = (k/k_1)^{n_{T1}}$ for $k < k_1$ and $\mathcal{P}_h(k) = \mathcal{P}_h^{\rm fid}$ for $k \le k_1$, which resembles predictions of an open inflation model associated

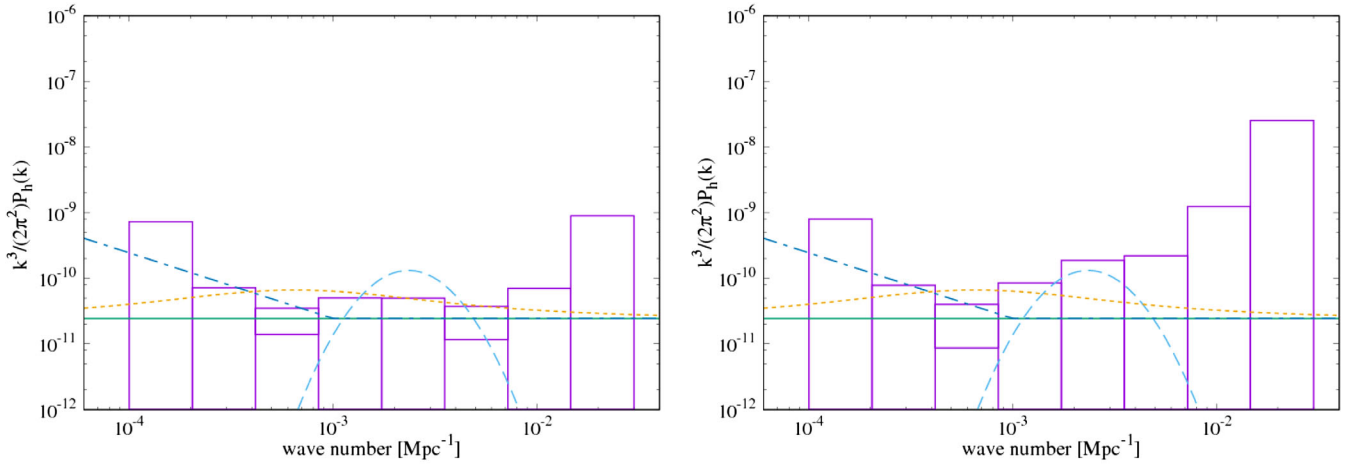

(a) "low-noise" : $(w_p^{-1/2}, \lambda) = (1\ \mu\mathrm{K}\cdot\mathrm{arcmin}, 1)$

(b) "high-noise" : $(w_p^{-1/2}, \lambda) = (10\ \mu\mathrm{K}\cdot\mathrm{arcmin}, 1)$

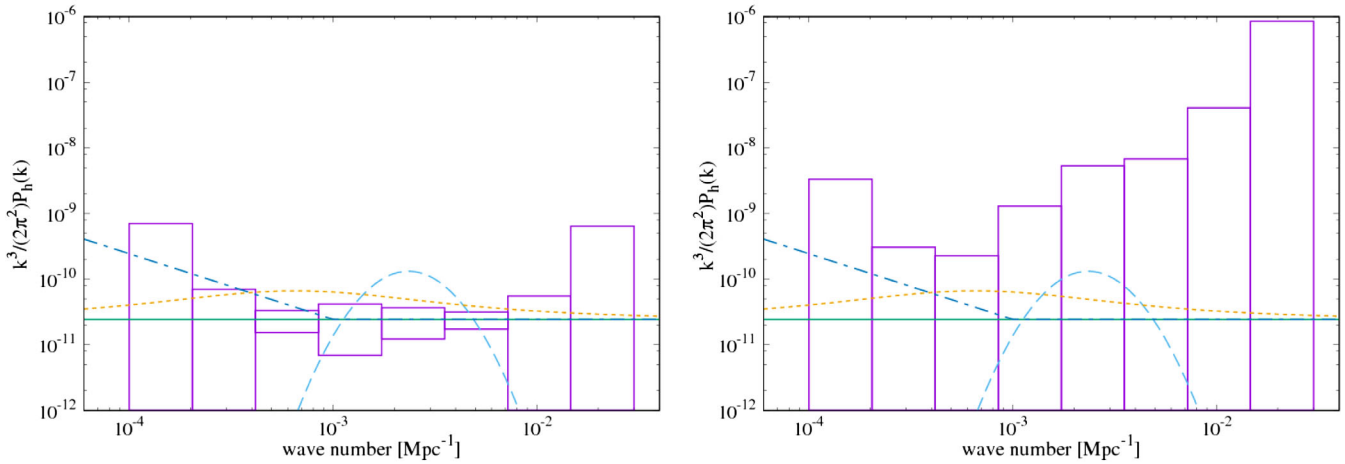

(c) "delensed" : $(w_p^{-1/2}, \lambda) = (1\ \mu\mathrm{K}\cdot\mathrm{arcmin}, 0)$

(d) "Planck" : $(w_p^{-1/2}, \lambda) = (63.1\ \mu\mathrm{K}\cdot\mathrm{arcmin}, 1)$

FIG. 2. Uncertainty of the reconstructed tensor power spectrum from B-mode observations. The fiducial model has $r = 0.01$ and $n_T = 0$, and the reconstruction parameters are $k_0 = 10^{-4}$ Mpc^{-1}, $k_N = 3 \times 10^{-2}$ Mpc^{-1}, and $N = 8$. (Top left) low-noise case. (Top right) high-noise case. (Bottom left) low noise with complete delensing. (Bottom right) Planck noise case. The solid line shows the fiducial spectrum; the dashed line is an example spectrum from the SU(2)-axion model with $r_* = 0.05$, $k_p = 2.0 \times 10^{-3}$ Mpc^{-1}, and $\sigma = 0.4$ [13]; the dotted line shows a massive gravity inflation model with $(\alpha, \beta, N_*, T_{\mathrm{reh}}) = (0.7, 1.0, 47, 10^{10}\ \mathrm{GeV})$; and the dot-dashed line shows a red-tilted spectrum on large scales with $(k_1, n_{T1}) = (10^{-3}\ \mathrm{Mpc}^{-1}, -1.0)$.

with a bubble nucleation [25]. For an example, we show the spectrum with $(k_1, n_{T1}) = (10^{-3}\ \mathrm{Mpc}^{-1}, -1)$. We emphasize that these parameter choices are not at all robust predictions of the models but serve only as examples.

To quantify how well we can distinguish models, we calculate the χ^2 statistic including the off-diagonal elements of the full covariance matrix. To this end, we calculate χ^2 as

$$\chi^2 = \sum_{i \le j}^{N} [\mathcal{P}_h^{\mathrm{fid}}(k_i) - \mathcal{P}_h^{\mathrm{model}}(k_i)] F_{ij} [\mathcal{P}_h^{\mathrm{fid}}(k_j) - \mathcal{P}_h^{\mathrm{model}}(k_j)], \tag{11}$$

and the probability to exceed (PTE) is defined as

$$P(\chi^2 > a, N) = \int_a^\infty P(\chi^2, N) d\chi^2. \tag{12}$$

Here, $P(x, n)$ is the χ^2 distribution function for n degrees of freedom,

$$P(x, N) = \frac{1}{2^{N/2}\Gamma(N/2)} x^{N/2-1} e^{-x/2}. \tag{13}$$

The PTE provides the probability to confuse the theoretically predicted models mentioned above with the fiducial power spectrum. For simplicity, we fix the theoretical model parameters and do not include them in the degrees of freedom.

TABLE II. Covariance matrix $(F^{-1})_{ij}$ for low-noise model with $N = 8$ and $f_{\rm sky} = 1$. The values enclosed in the boxes are the diagonal elements. The wave number of each bin is given by $k_n = \alpha^n k_0$, where $\alpha = (k_N/k_0)^{1/N} = 2.04$; see Eq. (1). One can obtain the covariance matrix with $f_{\rm sky} < 1$ by multiplying all the elements by $1/f_{\rm sky}$.

	$\delta\mathcal{P}_1$	$\delta\mathcal{P}_2$	$\delta\mathcal{P}_3$	$\delta\mathcal{P}_4$	$\delta\mathcal{P}_5$	$\delta\mathcal{P}_6$	$\delta\mathcal{P}_7$	$\delta\mathcal{P}_8$
$\delta\mathcal{P}_1$	$\boxed{4.9\times10^{-19}}$	-3.0×10^{-20}	2.9×10^{-21}	-2.7×10^{-21}	2.6×10^{-22}	-2.8×10^{-23}	5.2×10^{-23}	-8.8×10^{-22}
$\delta\mathcal{P}_2$	-3.0×10^{-20}	$\boxed{2.2\times10^{-21}}$	-2.5×10^{-22}	2.5×10^{-22}	-2.6×10^{-23}	3.1×10^{-24}	-5.6×10^{-24}	9.5×10^{-23}
$\delta\mathcal{P}_3$	2.9×10^{-21}	-2.5×10^{-22}	$\boxed{1.1\times10^{-22}}$	-1.7×10^{-22}	2.7×10^{-23}	-3.5×10^{-24}	6.2×10^{-24}	-1.0×10^{-22}
$\delta\mathcal{P}_4$	-2.7×10^{-21}	2.5×10^{-22}	-1.7×10^{-22}	$\boxed{6.7\times10^{-22}}$	-1.8×10^{-22}	2.5×10^{-23}	-4.2×10^{-23}	6.9×10^{-22}
$\delta\mathcal{P}_5$	2.6×10^{-22}	-2.6×10^{-23}	2.7×10^{-23}	-1.8×10^{-22}	$\boxed{6.5\times10^{-22}}$	-1.8×10^{-22}	2.8×10^{-22}	-4.3×10^{-21}
$\delta\mathcal{P}_6$	-2.8×10^{-23}	3.1×10^{-24}	-3.5×10^{-24}	2.5×10^{-23}	-1.8×10^{-22}	$\boxed{1.7\times10^{-22}}$	-4.8×10^{-22}	8.4×10^{-21}
$\delta\mathcal{P}_7$	5.2×10^{-23}	-5.6×10^{-24}	6.2×10^{-24}	-4.2×10^{-23}	2.8×10^{-22}	-4.8×10^{-22}	$\boxed{2.1\times10^{-21}}$	-3.9×10^{-20}
$\delta\mathcal{P}_8$	-8.8×10^{-22}	9.5×10^{-23}	-1.0×10^{-22}	6.9×10^{-22}	-4.3×10^{-21}	8.4×10^{-21}	-3.9×10^{-20}	$\boxed{7.5\times10^{-19}}$

TABLE III. χ^2 and PTE for various noise models, low noise, high noise, delensed, and Planck, which correspond to $(w_p^{-1/2}, \lambda) = (1.0, 1.0)$, (10.0,1.0), (1.0,0.0), and (63.1,1.0), respectively.

	Low noise		High noise		Delensed		Planck	
	χ^2	PTE	χ^2	PTE	χ^2	PTE	χ^2	PTE
SU(2) axion	1.5×10^{2}	9.3×10^{-28}	1.2×10^{1}	1.4×10^{-1}	6.3×10^{2}	1.6×10^{-131}	4.9×10^{-1}	1.0
Massive	1.2×10^{2}	1.4×10^{-21}	3.4×10^{1}	3.3×10^{-5}	3.6×10^{2}	7.7×10^{-73}	1.3	1.0
Red tilted	2.0×10^{1}	1.1×10^{-2}	1.6×10^{1}	4.3×10^{-2}	2.1×10^{1}	6.0×10^{-3}	1.7	9.9×10^{-1}
Null hypothesis	3.1×10^{2}	1.1×10^{-61}	2.1×10^{1}	7.0×10^{-3}	1.4×10^{3}	9.0×10^{-295}	5.7×10^{-1}	1.0

The values of χ^2 and PTE with $N = 8$ are tabulated in Table III. For reference, we also compute them for the Planck observation with the corresponding white noise, $w_p^{-1/2} = 63.1\ \mu\mathrm{K}\cdot\mathrm{arc\ min}$, which is obtained by averaging the noise band powers in 70, 100, and 148 GHz [26]. In the last row in Table III, we also show χ^2 for the null hypothesis, which is calculated by setting $\mathcal{P}_h^{\rm model}(k_i) = 0$ in Eq. (11). We find that Planck cannot detect the fiducial spectrum, and furthermore cannot distinguish the three theoretical predictions from it, since χ^2 is of order unity and the corresponding PTE is also unity. On the other hand, the future observations with $w_p^{-1/2} = 1\ \mu\mathrm{K}\cdot\mathrm{arc\ min}$ can distinguish the SU(2)-axion model and the massive gravity inflation model with high statistical significance, whereas the open inflation model is distinguished with moderate significance because of the cosmic variance at small wave numbers.

One may be surprised that we can distinguish the models despite the fact that the error bars appear larger than the differences between some models and the fiducial spectrum in Fig. 2. This is due to large correlations between the bins (see Table II). Indeed, ignoring the off-diagonal elements, i.e., $\sigma^2 = \sum_i^N F_{ii}[\mathcal{P}_h^{\rm fid}(k_i) - \mathcal{P}_h^{\rm model}(k_i)]^2$, we find that for $N \geq 8$ bins $\sigma^2 \ll \chi^2$. We also find that the values of σ^2 depend sensitively on the number of bins used, whereas those of χ^2 with off-diagonal terms do not. Only when the size of the bins is sufficiently large (see $N = 4$ in Table IV) do χ^2 and σ^2 agree because the bin-to-bin correlation is be suppressed in this case; thus, including the off-diagonal elements is essential.

So far, we have fixed the cosmological parameters. How would varying them change our results? Varying Ω_M and H_0 changes the distance to the last-scattering surface, shifting the B-mode power spectrum in the ℓ space. This would change the relationship between k and ℓ,

TABLE IV. Dependence of χ^2 and σ^2 on the number of bins for low-noise model.

	χ^2				σ^2			
	$N = 4$	$N = 8$	$N = 12$	$N = 16$	$N = 4$	$N = 8$	$N = 12$	$N = 16$
SU(2) axion	2.2×10^{3}	1.5×10^{2}	2.8×10^{2}	2.4×10^{2}	7.2×10^{2}	2.4×10^{1}	3.5×10^{1}	1.6×10^{1}
Massive	1.4×10^{2}	1.2×10^{2}	1.1×10^{2}	1.0×10^{2}	6.5×10^{1}	2.1×10^{1}	7.1	1.5
Red tilted	3.0×10^{1}	2.0×10^{1}	1.6×10^{1}	1.5×10^{1}	2.5×10^{1}	4.2	5.5×10^{-1}	1.9×10^{-2}
Null hypothesis	3.2×10^{2}	3.1×10^{2}	2.8×10^{2}	2.7×10^{2}	7.5×10^{1}	1.1×10^{1}	4.6	1.9

shifting features in the reconstructed tensor power spectra in the k space. Varying the optical depth τ changes the height of the reionization bump, which affects the amplitude of the reconstructed power at $k = k_{\rm reion} \approx 6 \times 10^{-4}$ Mpc^{-1}. However, in the era when we can make precise measurements of the B-mode power spectrum, these parameters will be determined so precisely that their impacts will not be the dominant uncertainty in the reconstructed power spectra.

We have also fixed our fiducial tensor power spectrum at a power-law power spectrum with $n_T \approx 0$. This is because this spectrum is motivated by single-field slow-roll inflation models, and detecting the difference from it would be a major discovery. Of course, we are free to use any spectra as the fiducial power spectrum.

IV. CONCLUSION

Reconstruction of the initial tensor power spectrum is complementary to the usual approach of forward modeling (i.e., to calculate the B-mode CMB power spectrum from a given initial tensor power spectrum) because we can test various models of the early Universe directly at the initial power spectrum level, without having to run Boltzmann solvers. In this paper, we have calculated the covariance matrix of the reconstructed tensor power spectra in bins of wave numbers. The χ^2 statistic [Eq. (11)] computed with this covariance matrix (given in Table II for the fiducial power spectrum with $r = 0.01$ and $n_T = 0$ and 1 μK · arc min noise) can be used to distinguish the tensor power spectra of one's favorite early Universe models from a power-law power spectrum. We find that reconstructed power spectra in bins of wave numbers are highly correlated and thus including the off-diagonal elements in χ^2 is essential in obtaining the correct answer.

We have tested our algorithm for three models, the SU(2)-axion model [13], massive gravity inflation (Appendix A), and open inflation [25], and found that future observations of CMB polarization by, e.g., LiteBIRD [23], should be able to distinguish the theoretical predictions of SU(2)-axion, open inflation, and massive gravity inflation models from a scale-invariant tensor power spectrum, depending on the model parameters. While we did not perform comprehensive parameter search for various models in this paper, we developed an interactive web tool to calculate χ^2 for any parameter values specified by users. This application is available online at http://numerus.sakura.ne.jp/research/open/srec/srec.php. We describe this tool in Appendix B. The web tool returns the covariance matrix, the χ^2 values, and the PTE and draws figures such as Fig. 2.

ACKNOWLEDGMENTS

This work was initiated at the first annual symposium of the Innovative Area "Why Does the Universe Accelerate?—Exhaustive Study and Challenges for the Future" held at the High Energy Accelerator Research Organization (KEK) March 8–10, 2017 and was completed at the symposium of the Yukawa International Seminar (YKIS2018a) "General Relativity—The Next Generation," held at Yukawa Institute for Theoretical Physics in Kyoto University February 19–23, 2018. This work was supported in part by JSPS KAKENHI Grants No. JP16H01098 (T. H.), No. JP15H05896 (E. K.), No. JP15H05891 (M. H.), and No. JP15H05888 (M. S.). T. H. was also supported by MEXT-Supported Program for the Strategic Research Foundation at Private Universities, 2014–2018 (Grant No. S1411024).

APPENDIX A: MASSIVE GRAVITY INFLATION

We consider the inflationary massive gravity theory with the mass term that depends on dynamics of inflation,

$$m_g^2 = f(\phi, \dot{\phi}). \tag{A1}$$

Depending on the form of the function f, it may vary substantially during inflation.

The equation of motion for the tensor perturbation takes the form

$$\ddot{\gamma} + 3H\dot{\gamma} + \left(\frac{k^2}{a^2} + m_g^2\right)\gamma = 0. \tag{A2}$$

Assuming a very small slow-roll parameter $\epsilon = -\dot{H}/H^2$, we obtain

$$\frac{d^2\gamma}{dn^2} + 3\frac{d\gamma}{dn} + \left(\frac{k^2}{a^2H^2} + \frac{m_g^2}{H^2}\right)\gamma = 0, \tag{A3}$$

where $dn = Hdt$. We set $n = n_f$ at the end of inflation. On superhorizon scales, assuming $m_g^2/H^2 \ll 1$, the above equation is solved to give the amplitude at the end of inflation as

$$\gamma_k(n_f) = \gamma_k(n_k) \exp\left[-\int_{n_k}^{n_f} \frac{m_g^2}{3H^2} dn\right], \tag{A4}$$

where n_k is the time at which the mode crosses the horizon, $k^2/a^2 = H^2$, the rms amplitude of which is $\langle \gamma_k^2(n_k) \rangle \propto H^2$ as usual. Thus, the spectrum at the end of inflation is given by

$$P_T(k; n_f) \propto \exp\left[-\int_{n_k}^{n_f} \frac{2m_g^2}{3H^2} dn\right], \tag{A5}$$

where $n_f - n_k = \ln(k_f/k)$ and $k_f = a(n_f)H$.

Now, let us assume the time dependence of m_g^2 as

$$\frac{2m_g^2}{3H^2} = n_{T*} + \beta\alpha \frac{\sinh \alpha n}{\cosh^2 \alpha n}, \tag{A6}$$

where we assume $\alpha \lesssim 1$ but β is arbitrary. We can then easily integrate it to find

$$\exp\left[-\int_{n_k}^{n_f}\frac{m_g^2}{3H^2}dn\right] = \exp\left[-n_{T*}N_k + \frac{\beta}{\cosh\alpha(N_k - N_*)} - \frac{\beta}{\cosh\alpha N_*}\right], \tag{A7}$$

where $N_k = n_f - n_k = -\ln(k/k_f)$ is the number of e-folds counted backward from the end of inflation and $N_* = n_f$ is the time at which the feature in the spectrum appears. Since we assumed $\alpha \lesssim 1$ and we want N_* to be fairly large $N_* \gtrsim 40$–50 to have an observable feature, the last term in the exponent is completely negligible. Thus, we obtain

$$P_T(k; n_f) \propto \exp\left[-n_{T*}N_k + \frac{\beta}{\cosh\alpha(N_k - N_*)}\right] = \left(\frac{k}{k_f}\right)^{n_{T*}} \exp\left[\frac{\beta}{\cosh\alpha(N_k - N_*)}\right]. \tag{A8}$$

Thus, the spectrum is the product of a power-law component and a factor peaked at $N = N_*$. The enhancement factor is e^β relative to the baseline.

APPENDIX B: USER'S MANUAL OF SPECTRUM RECONSTRUCTOR

We developed a web tool, SPECTRUM RECONSTRUCTOR,[4] to compute the Fisher matrix of reconstructed initial tensor power spectra. In this section, we provide a brief instruction of this tool.

SPECTRUM RECONSTRUCTOR assumes the cosmological parameters given in Table I. It returns a Fisher matrix and a covariance matrix and makes a plot of the fiducial power spectrum of tensor perturbations with error bars where the fiducial spectrum is assumed to be a power law given in Eq. (2).

The covariance matrix is then used to compute χ^2 and the PTE for various early Universe models. Three kinds of model power spectra that are introduced in the main text are provided in the tool as built-in models. One can also upload numerical data of a power spectrum as a custom model.

In the main page of the tool, we define the parameters controlling the Fisher analysis and plots, which are categorized into four tabs: "Basic," "Drawing," "Built-in models," and "Custom models." One can get information on each parameter in these tabs when one hovers over parameter names. In the Basic tab, one can specify the amplitude and the spectral index of the fiducial spectrum, the number of bins, and noise sources. In the Drawing tab, one can adjust the vertical and horizontal axes of the plot as well as the scale (logarithmic or linear). In the Built-in models tab, one can set the model parameters of SU(2)-axion, open inflation, and the massive gravity models that are introduced in the main text and also select the presence or absence of each model spectrum in the plot. Finally, in the Custom models tab, one can upload one's favorite power spectrum data in a simple text format.

After setting the parameters, clicking the "MAKE PLOT" button generates a plot in the portable network graphics (PNG) format. If one selects the presence of some model spectra, the corresponding χ^2's and PTEs are also tabulated below the plot. The Fisher and covariance matrices are provided in the text format at the link below the plot. This text file contains four blocks: the first two blocks are the Fisher matrices with and without the cosmic variance, and the remaining ones are the corresponding covariance matrices. The parameters and results including the uploaded spectrum, if it exists, are preserved for a few days on the system.

Note that the specifications and appearance of our web tool are subjected to change without prior notice for improvement.

[4] http://numerus.sakura.ne.jp/research/open/srec/srec.php.

[1] U. Seljak and M. Zaldarriaga, Phys. Rev. Lett. **78**, 2054 (1997).
[2] M. Kamionkowski, A. Kosowsky, and A. Stebbins, Phys. Rev. Lett. **78**, 2058 (1997).
[3] U. Seljak and M. Zaldarriaga, Astrophys. J. **469**, 437 (1996).
[4] A. Lewis, A. Challinor, and A. Lasenby, Astrophys. J. **538**, 473 (2000).
[5] D. Blas, J. Lesgourgues, and T. Tram, J. Cosmol. Astropart. Phys. 07 (2011) 034.
[6] R. Brout, F. Englert, and E. Gunzig, Ann. Phys. (N.Y.) **115**, 78 (1978).
[7] A. A. Starobinsky, Phys. Lett. **91B**, 99 (1980).
[8] K. Sato, Mon. Not. R. Astron. Soc. **195**, 467 (1981).
[9] A. H. Guth, Phys. Rev. D **23**, 347 (1981).
[10] A. Albrecht and P. J. Steinhardt, Phys. Rev. Lett. **48**, 1220 (1982).
[11] A. D. Linde, Phys. Lett. **108B**, 389 (1982).
[12] A. A. Starobinsky, Pis'ma Zh. Eksp. Teor. Fiz. **30**, 719 (1979) [JETP Lett. **30**, 682 (1979)].

[13] E. Dimastrogiovanni, M. Fasiello, and T. Fujita, J. Cosmol. Astropart. Phys. 01 (2017) 019.
[14] L. F. Abbott and M. B. Wise, Nucl. Phys. **B244**, 541 (1984).
[15] T. Tanaka and M. Sasaki, Prog. Theor. Phys. **97**, 243 (1997).
[16] G. Domnech, T. Hiramatsu, C. Lin, M. Sasaki, M. Shiraishi, and Y. Wang, J. Cosmol. Astropart. Phys. 05 (2017) 034.
[17] P. A. R. Ade *et al.* (Planck Collaboration), Astron. Astrophys. **594**, A13 (2016).
[18] M. Zaldarriaga and U. Seljak, Phys. Rev. D **58**, 023003 (1998).
[19] T. Namikawa and R. Nagata, J. Cosmol. Astropart. Phys. 10 (2015) 004.
[20] A. Lewis and A. Challinor, Phys. Rep. **429**, 1 (2006).
[21] N. Katayama and E. Komatsu, Astrophys. J. **737**, 78 (2011).
[22] B. Thorne, T. Fujita, M. Hazumi, N. Katayama, E. Komatsu, and M. Shiraishi, Phys. Rev. D **97**, 043506 (2018).
[23] T. Matsumura *et al.*, J. Low Temp. Phys. **176**, 733 (2014).
[24] M. Zaldarriaga, Phys. Rev. D **55**, 1822 (1997).
[25] D. Yamauchi, A. Linde, A. Naruko, M. Sasaki, and T. Tanaka, Phys. Rev. D **84**, 043513 (2011).
[26] J. Tauber *et al.* (Planck Collaboration), arXiv:astro-ph/0604069.